Asociación Argentina
de Mecánica Computacional

Mecánica Computacional Vol XXXV, págs. 595-618 (artículo completo)
Martín I. Idiart, Ana E. Scarabino y Mario A. Storti (Eds.)
La Plata, 7-10 Noviembre 2017

STOCHASTIC WIND-LOAD MODEL FOR BUILDING VIBRATION ESTIMATION USING LARGE-EDDY CFD SIMULATION AND RANDOM TURBULENC FLOW GENERATION ALGORITHMS

[a,b]**José A. Inaudi and** [c]**Carlos G. Sacco**

[a]*Departamento de Aeronáutica, Facultad de Ciencias Exactas, Físicas y Naturales, Universidad Nacional de Córdoba, Av. Velez Sársfield 1611, 5000 Córdoba, Argentina,*
http://www. www.efn.uncor.edu

[b]*Sirve Argentina Engineering Consulting,*
Córdoba, Argentina,
inaudijose@gmail.com

[c]*Departamento de Mecánica Aeronáutica, Facultad de Ingeniería IUA,*
Av. Fuerza Aérea 6500, Córdoba, Argentina
http://www. www.iua.edu.ar

Keywords: wind, turbulence, large eddy simulation, structural vibrations

Abstract. The application of computer fluid dynamics to the estimation of a stochastic wind loading model for vibration analysis of flexible buildings is studied in this paper. Large-Eddy-Simulation with random turbulence field as inflow boundary condition is used for estimating along the wind forces, across the wind forces and torsional moments along the height of the building. The stochastic turbulence of the inlet flow is modeled using techniques proposed in the literature and variations suggested by the authors, and along the wind and along the wind forces and torsional moments applied along the building height are estimated with sampled random processes resulting from the CFD analyses. The application of this numerical technique during the design stage of a concrete-wall 36-storey building with a parallelogram-shape plan is described. This structure is prone to high floor accelerations due to wind loading, compromising occupant comfort. The construction of random loading models for this building considering time and space correlation of forces and torsional moments is discussed and the use of the random loading to the design process of supplemental damping devices for the building is described.

1 INTRODUCTION

This paper presents an application of large eddy simulation (LES) for dynamic performance assessment of building structures subjected to wind loading. The application of algorithms for stochastic atmospheric turbulence generation at the inlet of the computational fluid finite element model is described and the stochastic characteristics of the artificially generated forcing signals are analyzed. The methodology is applied in the design process of a concrete shear wall building subjected to wind to estimate occupant comfort and supplemental damping design.

The structural project and reasons that motivated this study are presented in the second section. Random turbulence field generation algorithms to model the atmospheric boundary layer in the computational are presented in the third section. The main characteristics of the CFD software, fluid model used for the simulation, and the computed wind force signals for dynamic structural analysis are described in the fourth section. The response of the building to a simulated one-year recurrence wind scenario is presented and the performance improvement in peak total acceleration and peak floor angular velocity achieved with viscous and friction dampers are presented in the fifth section. Concluding remarks and further lines for future research work are defined in the last section.

2 PROJECT AND MOTIVATION

The structural project that motivated the present study is a new concrete-wall tower building comprising 36 levels above ground and 3 basement levels below ground to be built in an urban area of the city of Córdoba, Argentina. The residential tower was design by architect Morini. Structural engineers Fragueiro and Novillo led the structural engineering team.

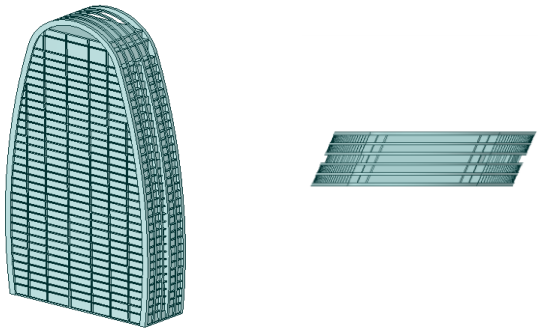

Figure 1 Elevation views of the building and plan of 5th story.

An elevation view of the building and a plan of the 5th story are shown in Figure 1. The height of the building above ground is 113 m; the 5th story plant dimensions are 63 m by 14 m. The first five fundamental periods of the structure are: 3.82 s (0.26 Hz), 3.36 s, 2.84 s, 0.95 s, 0.91 s. The first torsional mode shows a relatively large natural period (2.84 s).

Given that several natural frequencies of the structure are located on the range of relevant frequency content of wind forces, the structural engineer in charge of the project considered that the performance of the building under one-year recurrence wind action might be unsatisfactory. The main objective of the consultancy work that provided the results reported

herein was to assess occupant comfort for one-year return period wind and to design a wind-induced-vibration control system for the building to achieve the performance required according by the following human comfort criteria (defined by the client):

Table 1 Human occupant comfort criterion defined.

Performance measure	Criterion	Maximum Value
1 year return period Peak Acceleration	W.H. Melbourne (1988)	10.2 milli g
1 year return period Peak rotational velocity	Isyumov (1995)	1.5 milli rad/s

A more stringent performance criterion could have been defined for this residence building using ISO 101137 (2007) as shown in Figure 2. In this case the peak acceleration for 1-year return period events would have been 7.6 milli g.

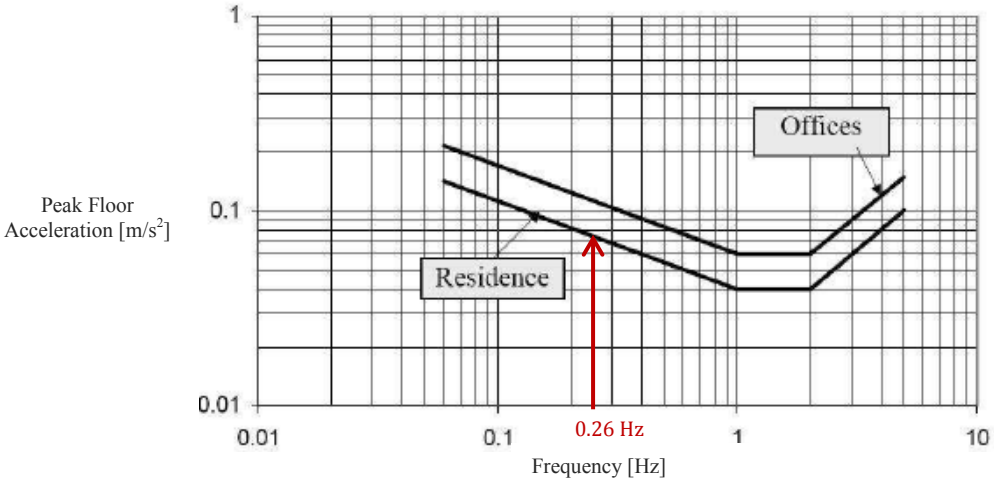

Figure 2 ISO 10137 occupant comfort criterion defined for mean peak combined floor acceleration.

Other important objectives for the development of the work reported were: (i) To comply with current architectural layout with minor structural system modifications (ii) To provide a solution with a cost efficient design.

No considerations are done on the safety of the structure subjected to maximum credible wind or earthquake effects because the structural engineer in charge of the project verified structural safety without added dampers.

The methodology for performance estimation and damper design are depicted in Figure 3. Because wind tunnel tests were not available for this project, a computer fluid dynamic model was developed using large eddy simulation (LES) and random wind turbulence simulation at the inlet by the authors to create random wind loading samples to be used for building performance assessment and damper design. A reduced-order structural model was created from an ETABS® structural model available, and the response of the building to wind loading was estimated by numerical simulation, computing peak floor total accelerations (PFTA) and peak floor angular velocities (PFAV) for a 10-minute (600 s) event. The structural model was

modified to include damper forces in the case of estimation of performance for various damper configurations analyzed.

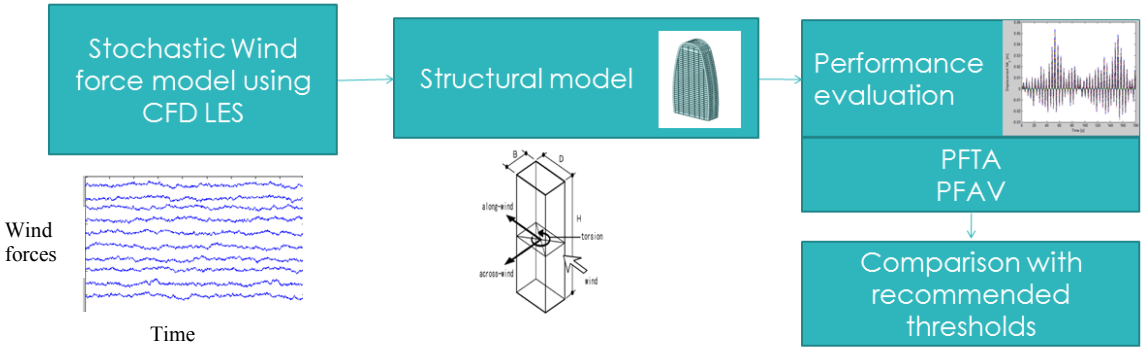

Figure 3 Diagram of the methodology for performance estimation.

3 STOCHASTIC WIND MODEL

We define INTI CIRSOC 102 mean wind speed profile:

$$U_x(z) = V\,\bar{b}\,(\frac{z}{10})^{\bar{\alpha}} \tag{1}$$

taking V = 25 m/s (defined by the structural engineer for a 1-year return period wind event), $\bar{\alpha}$ = ¼ and $\bar{b}$ = 0.45; z is the height measured from ground in meters.

Along-the-wind turbulence intensity was defined according as

$$I_{u_x}(z) = c\,(\frac{10\text{ m}}{z})^{1/6} \tag{2}$$

For the building location, two scenarios were considered by the structural engineer: $c = 0.30$ and $c = 0.20$. Damper design for $c = 0.20$ is reported herein.

Y and *Z* turbulence intensities are modeled as:

$$I_{u_y}(z) = 0.5 I_{u_x}(z) \tag{3}$$

$$I_{u_z}(z) = 0.5 I_{u_x}(z) \tag{4}$$

Turbulence power spectral densities (PSDs) of turbulence in the X, Y and Z directions are assumed using Von Karman models:

$$S_{u_x}(z,f) = \frac{4(I_{u_x}(z)U_x(z))^2(\frac{L_{u_x}(z)}{U_x(z)})}{\left[1+70.8\,(f\frac{L_{u_x}(z)}{U_x(z)})^2\right]^{5/6}} \tag{5}$$

$$S_{u_y}(z,f),= \frac{4(I_{u_y}(z)U_x(z))^2(\frac{L_{u_y}(z)}{U_x(z)})[1+188.4\left(2f\frac{L_{u_y}(z)}{U_x(z)}\right)^2]}{\left[1+70.8\,(f\frac{L_{u_y}(z)}{U_x(z)})^2\right]^{11/16}} \quad (6)$$

$$S_{u_z}(z,f) = \frac{4(I_{u_z}(z)U_x(z))^2(\frac{L_{u_z}(z)}{U_x(z)})[1+188.4\left(2f\frac{L_{u_z}(z)}{U_x(z)}\right)^2]}{\left[1+70.8\,(f\frac{L_{u_z}(z)}{U_x(z)})^2\right]^{11/16}} \quad (7)$$

Where f is frequency in Hz and $L_{u_x}, L_{u_y}, L_{u_z}$ are integral length scales for turbulence in directions X, y and Z, respectively. L_{u_x} is defined for the exposure condition of the building (INTI CIRSOC 2005) as

$$L_{u_x}(z) = l\,(\frac{z}{10\text{ m}})^{\bar{\varepsilon}} \quad (8)$$

with $l = 98\,m$ and $\bar{\varepsilon} = \frac{1}{3}$. Y and Z wind turbulence length scales were taken as

$$L_{u_y}(z) = 0.5L_{u_x}(z) \quad (9)$$

$$L_{u_z}(z)(z) = 0.5L_{u_x}(z) \quad (10)$$

Table 1 shows the main wind parameters assumed for the wind condition at different heights z measured from ground level.

Table 1 Main wind parameters

z [m]	$U_x(z)$ [m/s]	$I_{u_x}(z)$ c=0.2	$I_{u_x}(z)$ c=0.3	$L_{u_x}(z)$ [m]
1	6	0.29	0.44	45.49
5	9	0.22	0.34	77.78
10	11	0.20	0.30	98.00
20	13	0.18	0.27	123.47
50	17	0.15	0.23	167.58
100	20	0.14	0.20	211.13
113	21	0.13	0.20	219.91

Wind turbulence is modeled as random processes with $I_{u_x}(z)$, $I_{u_y}(z), I_{u_z}(z)$, PSD Von Karman with integral length scales $L_{u_x}(z), L_{u_y}(z), L_{u_z}(z)$ and turbulence spatial coherence adjusted to Davenport model:

$$coh(y_1, z_1, y_2, z_2, f) = e^{-12\, f \frac{\sqrt{(y_2-y_1)^2+(z_2-z_1)^2}}{\frac{1}{2}(U_x(z_1)+U_x(z_2))}} \tag{11}$$

Wind velocity field simulation at the inlet for LES model implementing Huang's random field generation (RFG) (Huang et al, 2010). As indicated by Castro et al. Huang's method is based on Smirnov's and Kraichnan's method (Castro et al., 2016; Smirnov et al., 2001; Kraichnan, 1970).

The methodology proposed by Huang, called DSRFG (for discretizing and synthesizing random flow generation) produces random 3-dimensional turbulence realizations for fluctuating velocity from any prescribed power spectral densities for the *X*, *Y* and *Z* random velocity components. A random velocity field realization can be synthesized as

$$u_i(\boldsymbol{x}, t) = \sum_{m=1}^{M} \sum_{n=1}^{N} p_i^{m,n} \cos\left(\tilde{k}_j^{m,n} \tilde{x}_j + \omega_{m,n}\, t\right) + q_i^{m,n} \sin\left(\tilde{k}_j^{m,n} \tilde{x}_j + \omega_{m,n}\, t\right) \tag{12}$$

Where $u_i(\boldsymbol{x}, t)$ is the i-th Cartesian component of the velocity field, $\boldsymbol{x}$ the position vector,

$$p_i^{m,n} = sgn(r_i^{m,n}) \sqrt{\frac{4}{N} S_i(z, f_m) \frac{(r_i^{m,n})^2}{1+(r_i^{m,n})^2}} \tag{13}$$

$$q_i^{m,n} = sgn(r_i^{m,n}) \sqrt{\frac{4}{N} S_i(z, f_m) \frac{1}{1+(r_i^{m,n})^2}} \tag{14}$$

Where $r_i^{m,n}$ is a standard Gaussian random sample with zero mean and unit variance. In Eq. 14 $S_i(z, f_m)$ is the one-sided power spectral density spectrum for level z defined for each frequency f_m considered in the random process realization, $f_o, f_o + \Delta f, f_o + 2\Delta f \ldots, f_{max}$.

$\omega_{m,n}$ are statistically independent realizations of a zero mean Gaussian random variable with standard deviation $2\pi f_m$.

The components of $\tilde{\boldsymbol{k}}^{m,n}$ must be computed as the soluction of a set of nonlinear algebraic to satisfy the incompressibility condition of the simulated flow. Defininig each normalized frequency $k_m = \frac{f_m}{\bar{U}_x(z)}$ the following nonlinear set of equations is solved to compute the auxiliary vector $\boldsymbol{k}^{n,m}$

$$|\boldsymbol{k}^{n,m}| = k_m \tag{15}$$

$$\boldsymbol{k}^{n,m} \cdot \boldsymbol{p}^{n,m} = 0 \tag{16}$$

$$\boldsymbol{k}^{n,m} \cdot \boldsymbol{q}^{n,m} = 0 \tag{17}$$

The components of $\tilde{\boldsymbol{k}}^{m,n}$ are computed as

$$\tilde{k}_j^{m,n} = \frac{k_j{}^{n,m}}{k_o} \tag{18}$$

where $k_o = \frac{f_o}{\bar{U}_x(z)}$.

$\tilde{x}_i$ is the i-th Cartesian component of the normalized position vector is defined as

$$\tilde{\boldsymbol{x}} = \boldsymbol{x}/L_s \tag{19}$$

where

$$L_s = \theta_1 \sqrt{L_{u_x}^2 + L_{u_y}^2 + L_{u_z}^2} \tag{20}$$

θ_1 is a parameter that is selected to fit the spatial correlation of turbulence.

Samples of the random velocity field components generated with the implemented algorithm are shown in Figure 4 for the Y and Z directions for a specific time ($t = 0$) and $x = 0$, $0 < Y < 200\,m$ and $0 < Z < 100\,m$.

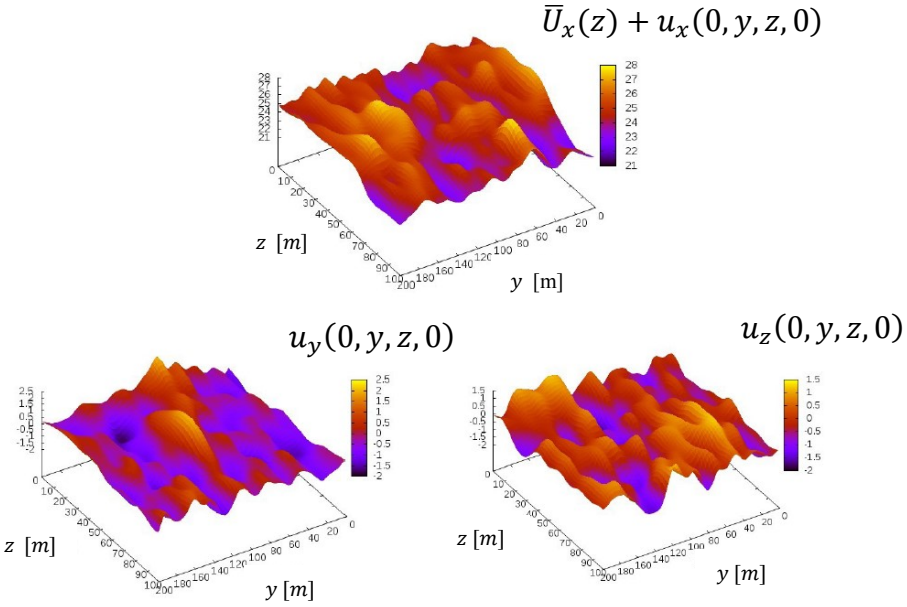

Figure 4 Tridimensional random turbulence generation samples at inlet of the FEM domain.

Spatial correlation of wind turbulence for different distances between points simulated and a comparison of theoretical coherence (green line) and estimated coherence of simulated signals (blue line) for two points separated by 20 m are shown in Figure 5.

Figure 6 compares PSD estimated using artificially generated samples ($f_o = 0.01\,Hz$, $\Delta f = 0.05\,Hz$, and $f_o = 4\,Hz$) vs. assumed Von Karman PSD. Frequency fit below 3 Hz is satisfactory. The RFG algorithm shows lower frequency content at the high frequency range compared with the target PSD but this is not relevant for this structure, because wind force rms components at frequencies larger than 4 Hz are very low in the atmospheric boundary layer and do not produce significant contributions to peak acceleration in the structure.

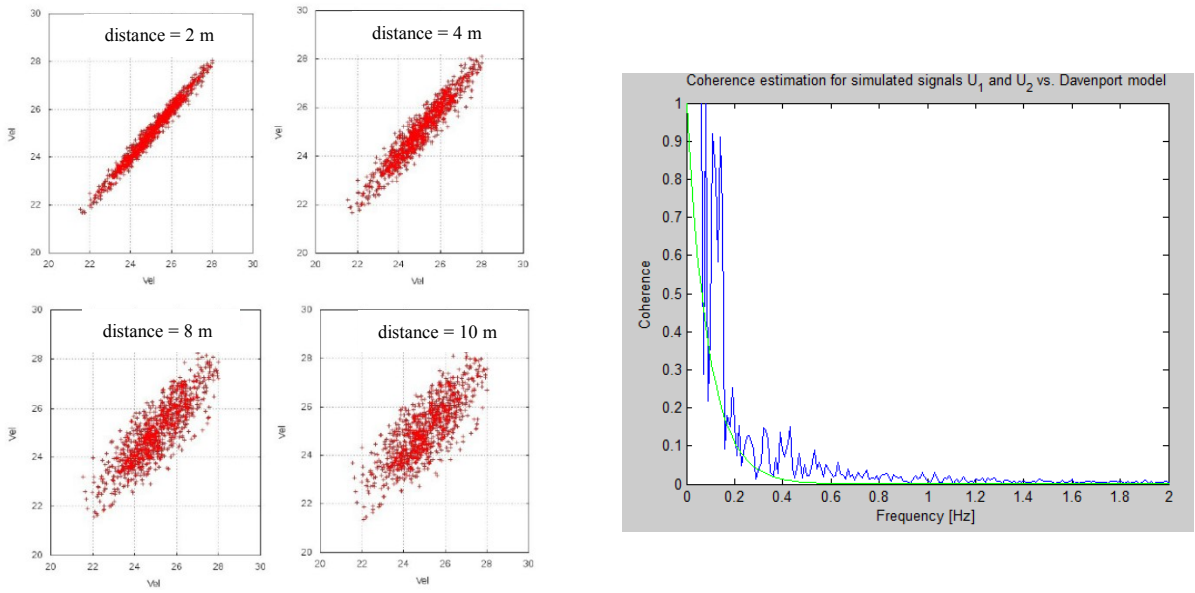

Figure 5 Spatial correlation and coherence of longitudinal turbulence samples ($\theta_1 = 0.5$).

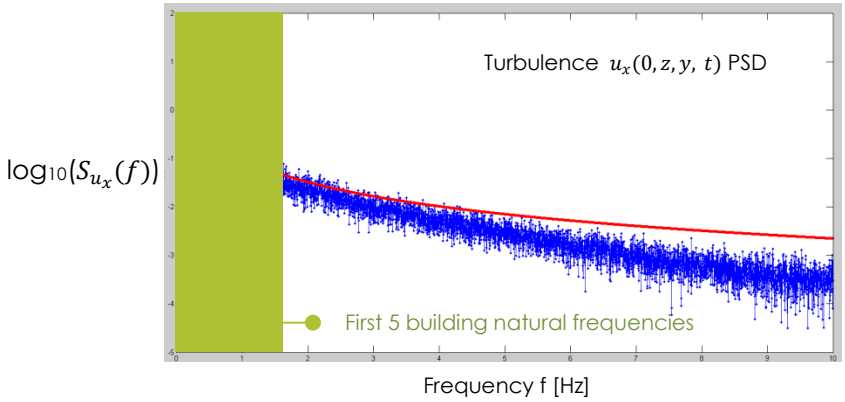

Figure 6 Samples PSDs for X-turbulence computed with Huang RFG algorithm vs. Von Karman target PSD.

Although not shown in figures, theoretical *Y* and *Z* turbulence PSDs assumed for the wind are adequately adjusted in the same frequency range.

4 CFD SOFTWARE, FLUID MODEL AND SIMULATED WIND FORCE SAMPLES

To simulate non stationary flow uncompressible linear viscous flow is modelled using Navier Stokes equations. These equations are complemented with a sub-grid scale model to simulate the turbulent flow behavior (Smagorinsky ,1963).

Given a uncompressible linear viscous fluid domain Ω with boundary Γ, the equations of motion and incompressibility condition can be derived as

$$\frac{\partial \boldsymbol{u}}{\partial t} + \boldsymbol{u}\cdot\boldsymbol{\nabla u} - \frac{\mu}{\rho}\boldsymbol{\nabla}^2\boldsymbol{u} + \frac{1}{\rho}\boldsymbol{\nabla} p = \boldsymbol{f} \ \text{ in } \Omega \times (t_o, t_f) \tag{21}$$

$$\boldsymbol{\nabla} \cdot \boldsymbol{u} = 0 \ \text{ in } \Omega \times (t_o, t_f) \tag{22}$$

where $\boldsymbol{u}(\boldsymbol{x}, t)$ is the velocity vector field, $p(\boldsymbol{x}, t)$ is the pressure field, ρ is the fluid density (assumed constant), μ is the viscosity constant, $\boldsymbol{f}$ is the force per unit mass (gravity acceleration vector in this case), $\boldsymbol{x}$ is the position vector, defined by Cartesian coordinates x, y and z in this analysis.

The boundary conditions of the model hold for $t \in (t_o, t_f)$, $t_o =$ initial and $t_f =$final simulation time.

$$\boldsymbol{u}(\boldsymbol{x}, t) = \bar{\boldsymbol{u}}(\boldsymbol{x}, t) \ \text{ in } \Gamma_{\boldsymbol{u}} \times (t_o, t_f) \tag{23}$$

$$[\boldsymbol{\sigma}(\boldsymbol{x}, t)] \cdot \hat{\boldsymbol{v}} = \bar{\boldsymbol{t}}(\boldsymbol{x}, t) \ \text{ in } \Gamma_{\boldsymbol{\sigma}} \times (t_o, t_f) \tag{24}$$

where $[\boldsymbol{\sigma}]$ is the stress tensor and $\hat{\boldsymbol{v}}$ is the unit vector normal at each point of the boundary surface. $\Gamma_{\boldsymbol{u}}$ and $\Gamma_{\boldsymbol{\sigma}}$ are the portions of the boundary where velocity field and stress tensor are specified.

Initial conditions are defined as

$$\boldsymbol{u}(\boldsymbol{x}, t_o) = \boldsymbol{u}_o(\boldsymbol{x}) \ \text{ in } \Omega \tag{25}$$

$$p(\boldsymbol{x}, t_o) = p_o(\boldsymbol{x}) \ \text{ in } \Omega \tag{26}$$

4.1 Fractioned Step Algorithm

Since the beginning of computational fluid dynamics (CFD) several algorithms have been proposed to solve or approximate the solution of the Navier Stokes equations for uncompressible fluid. Among these we can find the pressure correction approach (Chorin and Teman, 1968; Harlow and Welch, 1965; Kim and Moin, 1975 and Patankar,1981). These algorithms decompose the operators (convection, diffusion and incompressibility) at each time step of the simulation. Following this approach we obtain computational schemes that satisfy the inf-sup or Ladyzenskaja-Babuška-Brezzi (LBB) condition using the same interpolation functions for the velocity field and the pressure field.

In this work, the 3-step fractional step algorithm developed by Kin and Moin (Kim and Moin, 1975) was implemented for the solution of Navier Stokes equations.

The equation of motion is divided in a predictor and a corrector step:

$$\bar{\mathbf{u}}_{n+1} = \boldsymbol{u}_n + \delta t \left[\boldsymbol{u}_{n+\theta} \cdot \boldsymbol{\nabla} \boldsymbol{u}_{n+\theta} + \frac{\gamma}{\rho} \boldsymbol{\nabla} p_n - \frac{\mu}{\rho} \boldsymbol{\nabla}^2 \boldsymbol{u}_{n+\theta} + \boldsymbol{f}_{n+\theta} \right] \tag{27}$$

$$\boldsymbol{u}_{n+1} = \bar{\mathbf{u}}_{n+1} - \frac{\delta t}{\rho} (\boldsymbol{\nabla} p_{n+1} - \gamma \boldsymbol{\nabla} p_n) \tag{28}$$

The term $\bar{\mathbf{u}}_{n+1}$ is called fractional momentum and represents an approximation to the velocity

that does not satisfy the incompressibility condition (divergence of velocity field equal to zero). The parameter θ can define different time integration schemes such as $\theta = 0$ Euler forward, $\theta = 1$ Euler backwards, and $\theta = 1/2$ Cranck Nicholson). Parameter γ takes values 1 or 0 if the pressure is kept in the equation of fractional moment or not, respectively. In this work we selected $\theta = 0$ and $\gamma = 0$ to use Euler backwards method; this leads to a semi-implicit algorithm. The first and third steps are explicit, and the pressure computation is implicit.

Taking the divergence of Eq. 28 and forcing the incompressible condition:

$$\boldsymbol{\nabla^2}(p_{n+1} - \gamma p_n) = \frac{\rho}{\delta t}\boldsymbol{\nabla} \cdot \bar{\mathbf{u}}_{n+1} \tag{29}$$

This equation can be solved to compute the pressure at $n + 1$.

The geometric domain is discretized using the finite element (FE) method with a first-order scheme. Defining the projection of two vector fields as

$$\langle \boldsymbol{a}, \boldsymbol{b} \rangle = \int_\Omega \boldsymbol{a} \cdot \boldsymbol{b}\, d\Omega \tag{30}$$

and selecting test functions $({}_h\mathbf{v}\,,\, {}_hq) \in \mathbf{V}_h \times \mathrm{Q}_h$, the Galerkin weak form of the differential equations to be integrated yield for each time step, of duration δt, the following equations to be solved:

Step 1. Fractional Momentum

$$\frac{1}{\delta t}\langle {}_h\bar{\mathbf{u}}_{n+1},\ {}_h\mathbf{v}\rangle = \frac{1}{\delta t}\langle {}_h\boldsymbol{u}_n,\ {}_h\mathbf{v}\rangle - \langle {}_h\boldsymbol{u}_n \cdot \boldsymbol{\nabla}\, {}_h\boldsymbol{u}_n,\ {}_h\mathbf{v}\rangle - \frac{\mu}{\rho}\langle \boldsymbol{\nabla}\, {}_h\boldsymbol{u}_n, \boldsymbol{\nabla}\, {}_h\mathbf{v}\rangle - \langle \boldsymbol{f}_n,\ {}_h\mathbf{v}\rangle \tag{31}$$

Step 2. Pressure calculation

$$\langle \boldsymbol{\nabla}\, {}_hp_{n+1}, \boldsymbol{\nabla}\, {}_hq\rangle = \frac{\rho}{\delta t}\left[\langle {}_h\bar{\mathbf{u}}_{n+1} - {}_h\boldsymbol{u}_n, \boldsymbol{\nabla}\, {}_hq\rangle - \langle \boldsymbol{\nabla} \cdot {}_h\boldsymbol{u}_n,\ {}_hq\rangle\right] \tag{32}$$

Step 3. Velocity correction

$$\langle {}_h\boldsymbol{u}_{n+1},\ {}_h\mathbf{v}\rangle = \langle {}_h\boldsymbol{u}_n,\ {}_h\mathbf{v}\rangle - \frac{\delta t}{\rho}\langle \boldsymbol{\nabla}\, {}_hp_{n+1},\ {}_hq\rangle \tag{33}$$

Boundary conditions

Wind velocity boundary conditions are applied on the corrected velocities ${}_h\boldsymbol{u}_{n+1}$, while the pressure boundary conditions are imposed in Step 2.

4.2 Statibilization strategy

The discrete form of the convective terms produce numerical instabilities for high Reynolds numbers. For this reason, a stabilization scheme must be used to solve equation in Step 1. In this work we use the Orthogonal Subscale Stabilization method (OSS) (Codina, 2001) . In addition, the algorithm requires a stabilization applied to the incompressibility solution in Step 2) (Codina, 2001).

The complete algorithm can be described as

Step 1

$$\frac{1}{\delta t}\langle\, {}_h\bar{\mathbf{u}}_{n+1},\, {}_h\mathbf{v}\rangle = \frac{1}{\delta t}\langle\, {}_h\boldsymbol{u}_n,\, {}_h\mathbf{v}\rangle - \langle\, {}_h\boldsymbol{u}_n \cdot \boldsymbol{\nabla}\, {}_h\mathbf{u}_n,\, {}_h\mathbf{v}\rangle - \frac{\mu}{\rho}\langle \boldsymbol{\nabla}\, {}_h\boldsymbol{u}_n, \boldsymbol{\nabla}\, {}_h\mathbf{v}\rangle - \langle \boldsymbol{f}_n,\, {}_h\mathbf{v}\rangle - \langle \tau_1(\, {}_h\boldsymbol{u}_n \cdot \boldsymbol{\nabla}\, {}_h\mathbf{u}_n - \, {}_h\pi_n\,),\, {}_h\boldsymbol{u}_n \cdot \boldsymbol{\nabla}\, {}_h\mathbf{v}\ \rangle \quad (34)$$

Step 2

$$\langle \boldsymbol{\nabla}\, {}_hp_{n+1}, \boldsymbol{\nabla}\, {}_hq\rangle = \frac{\rho}{\delta t+\tau_2}\left[\langle\, {}_h\bar{\mathbf{u}}_{n+1} - \, {}_h\boldsymbol{u}_n, \boldsymbol{\nabla}\, {}_hq\rangle - \langle \boldsymbol{\nabla}\cdot\, {}_h\boldsymbol{u}_n,\, {}_hq\rangle\right] + \frac{\tau_2}{\delta t+\tau_2}\langle \boldsymbol{\nabla}\, {}_h\xi_n, \boldsymbol{\nabla}\, {}_hq\rangle \quad (35)$$

Step 3

$$\langle\, {}_h\boldsymbol{u}_{n+1},\, {}_h\mathbf{v}\rangle = \langle\, {}_h\boldsymbol{u}_n,\, {}_h\mathbf{v}\rangle - \frac{\delta t}{\rho}\langle \boldsymbol{\nabla}\, {}_hp_{n+1},\, {}_hq\rangle \quad (36)$$

Step 4

$$\langle\, {}_h\pi_n,\, {}_h\tilde{\mathbf{v}}\rangle = \langle\, {}_h\boldsymbol{u}_n \cdot \boldsymbol{\nabla}\, {}_h\mathbf{u}_n,\, {}_h\tilde{\mathbf{v}}\rangle \quad (37)$$

Step 5

$$\langle\, {}_h\xi_n,\, {}_h\tilde{\mathbf{v}}\rangle = \langle \boldsymbol{\nabla}\, {}_hp_n,\, {}_h\tilde{\mathbf{v}}\rangle \quad (38)$$

Where ${}_h\pi_n$ and ${}_h\xi_n$ are the projections of the convective terms and of the pressure gradients on the test functions subspace. The parameters τ_1 and τ_2 are defined and adjusted for each case under analysis.

The equations defined in Steps 1, 3, 4, and 5 are solved in an explicit scheme condensing the mass matrices. The system of equations in Step 2 is solved in an implicit scheme in the present work; the conjugate gradient method with a diagonal pre-conditioner is used in Step 2.

4.3 Turbulence modeling

The LES of the turbulent behavior of the flow is done using an experimental sub-grid scale turbulence model (Smagorinsky, 1963). When LES formulation is applied the viscous term in Step 1 is modified; instead of $\frac{\mu}{\rho}$ we use $\frac{\mu}{\rho} + \, {}_t\nu$ where ${}_t\nu$ is the so called turbulent viscosity

$$ {}_t\nu = C_s\Delta^2\sqrt{2S_{ij}S_{ij}} \quad (39)$$

where

$$S_{ij} = \frac{1}{2}\left(\frac{\partial u_i}{\partial x_j} + \frac{\partial u_j}{\partial x_i}\right) \quad (40)$$

The parameter $C_s = 0.1$ is the Smagorinsky coefficient and Δ is a characteristic dimension of the element (characteristic length of the FE grid).

4.4 FE mesh and integration time step

Figure 7 shows the FE (finite element) domain mesh used for the analysis. The volume has dimensions of 1200 m x 1200 m x 400 m in height. A total number of 6.3 million tetrahedral linear elements with refinement in the region of larger interaction with the building was defined. Element characteristic lengths are on the order of 0.6 m close to the building and 20 m far from the building. A sensibility analysis of estimated pressures on the building was carried out keeping the size (20 m) of the elements located far from the building and refining elements close to the building from 2 m to 0.3 m. Minor difference in pressure estimation was detected for elements smaller than 0.7 m, reason why 0.6 m was adopted for the elements close to the building.

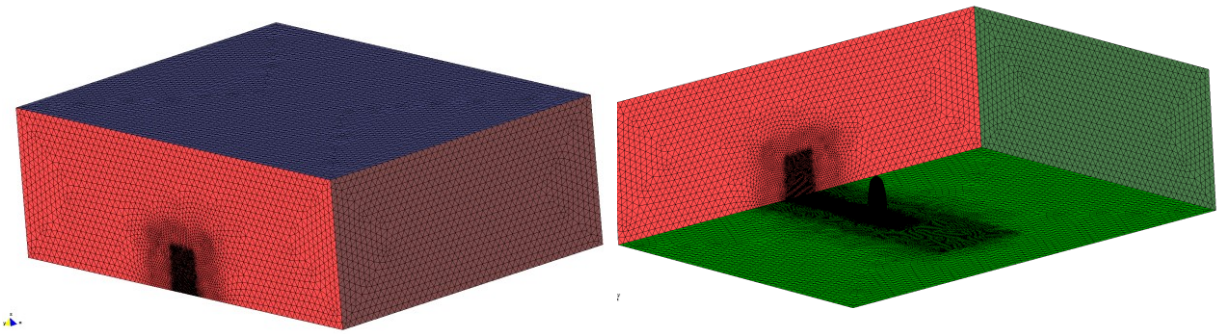

Figure 7 FE mesh employed for the LES CFD model of the building.

Although the integration algorithm can handle variable integration time steps, to simplify wind forces time series a fixed time step of 0.01 s was used. Numerical stability was assured with this time step with Courant number between 0.3 and 0.6 along the simulation of 800 seconds.

5 ESTIMATED WIND VELOCITIES AND PRESSURES

Figures 8 and 9 show the velocity field and pressure field at a specific instant for the wind acting in the direction perpendicular to the widest side of the building.

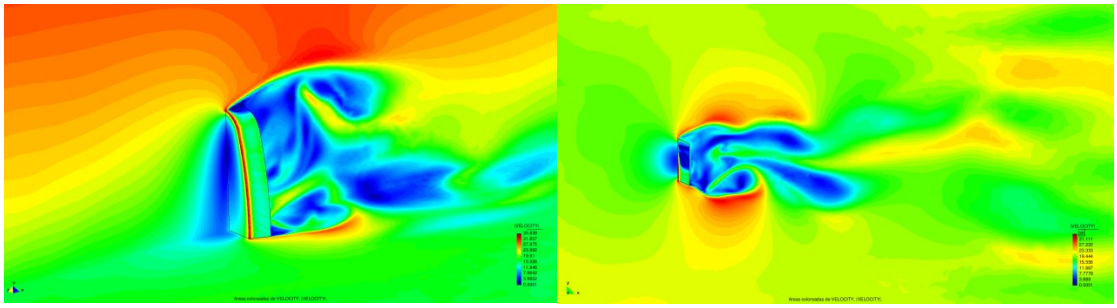

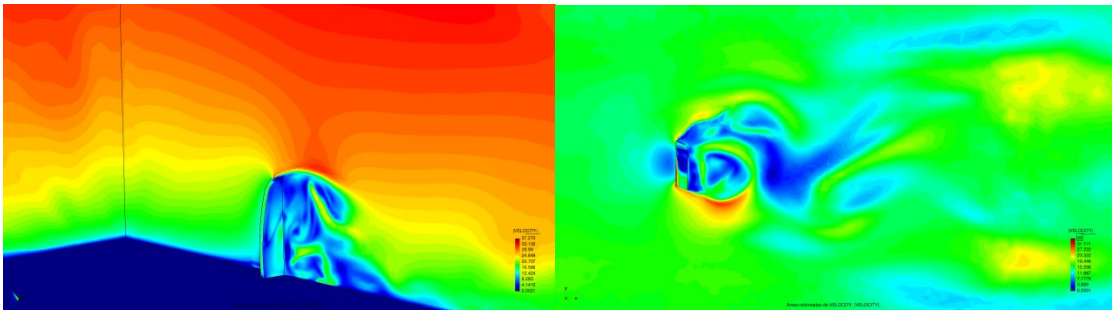

Figure 8 Instantaneous wind velocity fields for wind in the Y direction, simulating turbulent flow in the inlet using Huang algorithm and LES CFD solution of Navier Stokes equations.

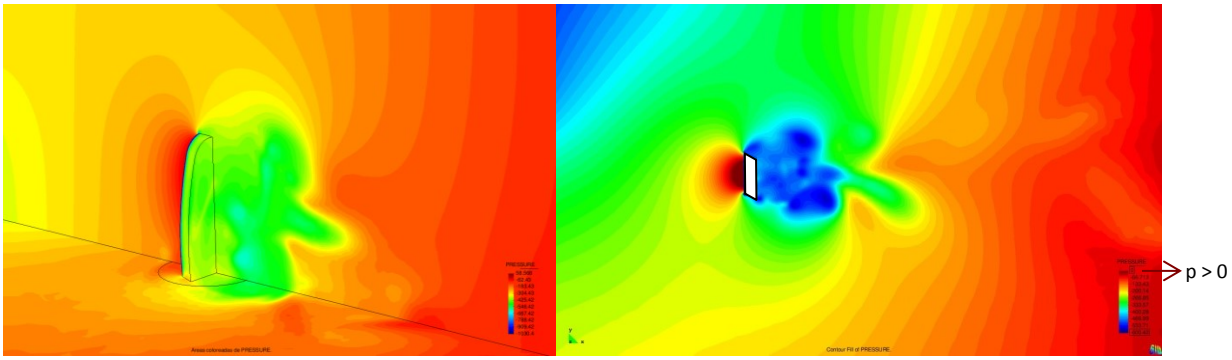

Figure 9 Instantaneous pressure field for wind in the Y direction, simulating turbulent flow in the inlet using Huang algorithm and LES CFD solution of Navier Stokes equations.

Figure 10 shows the base shear of the building due to wind acting in the Y direction as a function of time for two scenarios: with random wind turbulence in the inlet and with no turbulence in the inlet.

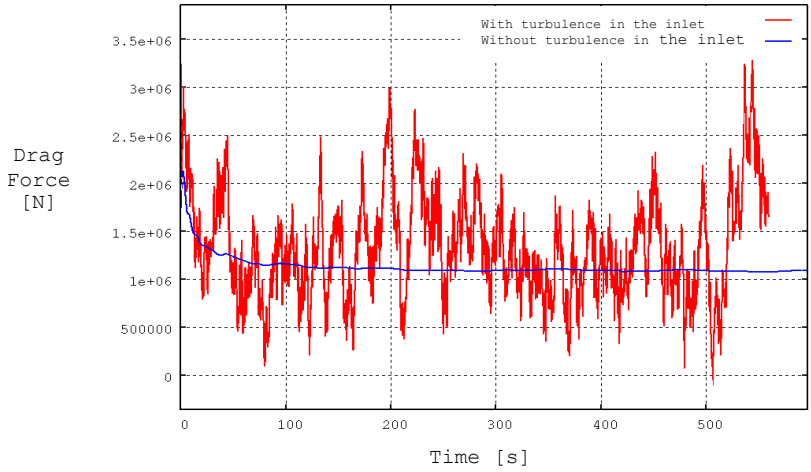

Figure 10 Total drag on the building (along the wind) for wind in the Y direction (perpendicular to the widest face of the building).

Integrating at each simulation time the stresses on the building surface, divided by portions at each level (building story) along the wind forces, across the wind forces, and torsional moments are computed to be used for dynamic performance estimation of the building.

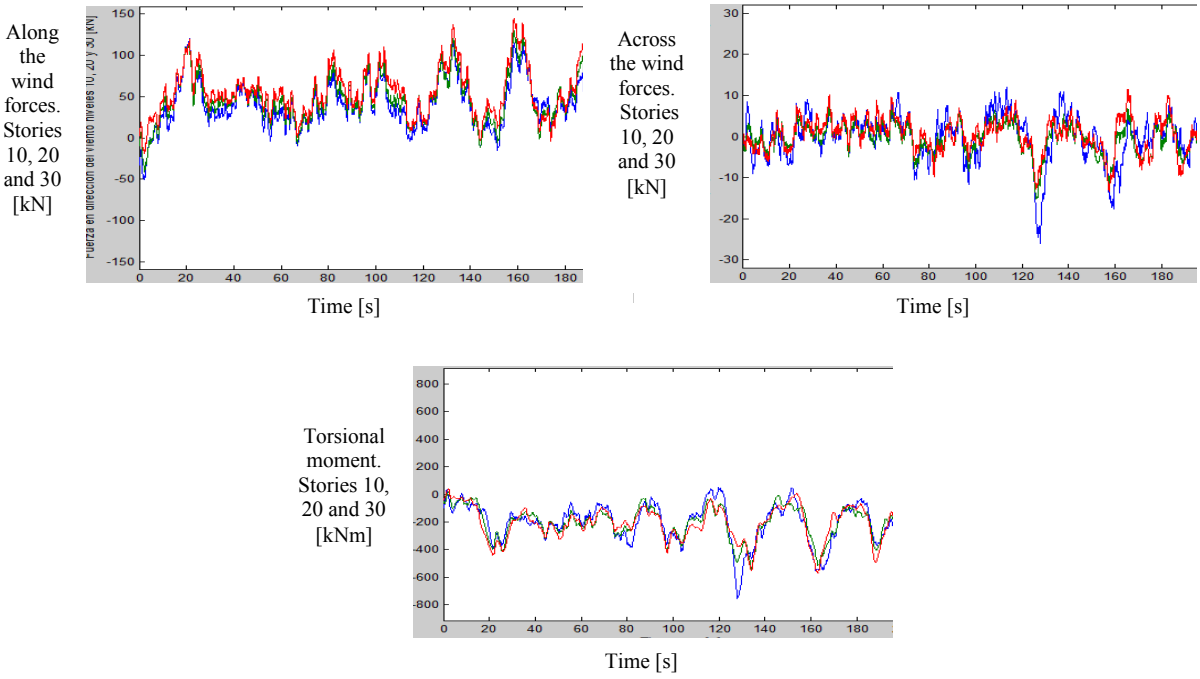

Figure 11 Along the wind, across the wind and Z-moment at levels 10, 20 and 30 for wind acting in the Y direction simulated using LES CFD solution and Huang algorithm RFG in the inlet.

6 BUILDING PERFORMANCE

The dynamic response of the building to the simulated wind load is estimated by numerical integration of the equations of motion of a reduced-order model of the building obtained from an ETABS® model used by the structural engineer. The reduced-order model considered 100 modal coordinates with 1% modal damping. Nodes N_1, N_2, N_3, N_4, and N_4, N_5 defined along the perimeter of the plan at each floor of the building were defined to compute peak accelerations.

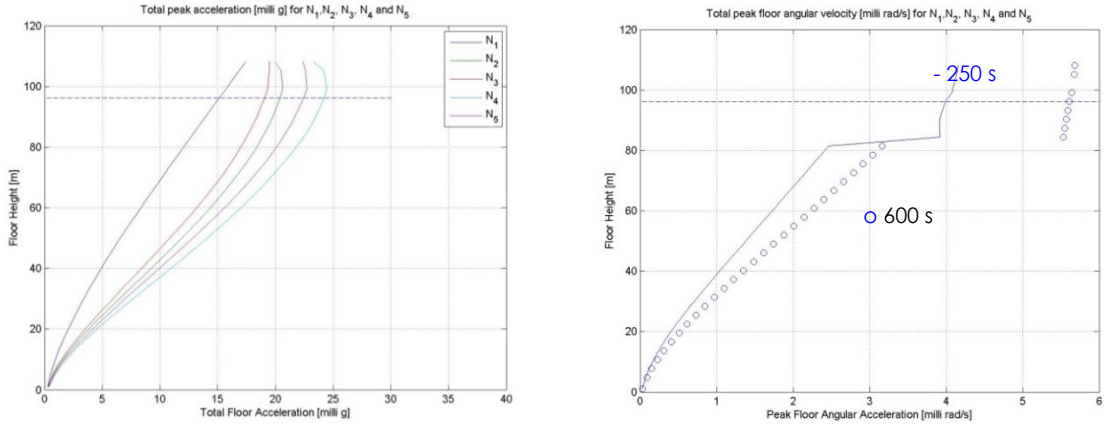

Figure 12 Estimated performance of the building with modal damping ratios of 0.01. Turbulence intensity defined for $c = 0.2$. Peak floor accelerations estimated for 600 s event and peak floor angular velocities estimated for 250 and 600 s event.

As shown in Figure 12, peak floor accelerations and peak floor angular velocities exceeded the recommended human comfort admissible values for a large portion of the building. The need of supplemental dampers was confirmed by this result. A discontinuity of concrete walls al level 28, determines a significant increment of the peak floor angular velocity between levels 28 and 29 (see Fig. 12b).

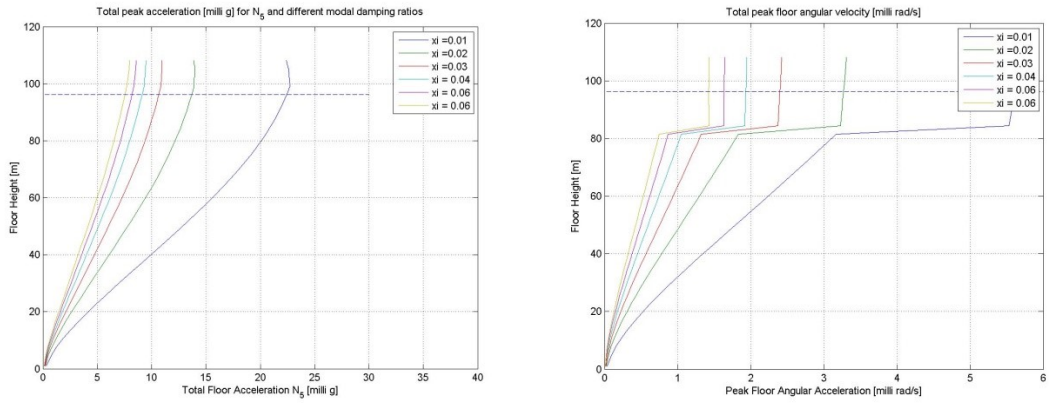

Figure 13 Estimated performance of the building with augmented modal damping ratios of 0.01, 0,02, 004, 0.04, 0.05 and 0.06. Wind turbulence intensity defined for $c = 0.2$.

To assess an order of magnitude of the required increment in modal damping ratios, a parametric analysis was performed simulating the response of the model subjected to random wind forces for values of modal damping ratios from 0.01 to 0.06. Estimated performance improvements due to modal damping augmentation are shown in Figure 13. Modal damping ratios above 4% reduce peak floor accelerations to values of the order of 10 milli g for turbulence intensity defined by parameter $c = 0.2$ (Eq. 2). These results indicated the convenience of supplemental dampers. Different damper intervention strategies were analyzed with the structural engineer and architect in charge of the project. The main results of the damper design process are presented in the following section.

7 DAMPER CONFIGURATION DESIGN

The following damper configurations were analyzed to improve the performance of the building:

- Supplemental linear viscous damper configurations:
  - I. 68 Diagonal bracing with linear viscous dampers connecting floors n and n+1
  - II. 32 diagonal bracing with linear viscous dampers connecting floors n and n+1 (at locations with larger total energy dissipation)
  - III. 34 diagonal bracing with linear viscous dampers connecting floors n and n+2
  - IV. 22 diagonal bracing with 22 linear viscous dampers connecting floors n and n+2 (at locations with larger total energy dissipation)
  - V. 35 diagonal bracing with linear viscous dampers connecting floors n and n+2 and additional 35 diagonal elastic bracing

- VI. 22 diagonal bracing with linear viscous dampers connecting floors n and n+2 and additional 22 diagonal elastic bracing

- Supplemental friction damper configuration:
  - VII. 20 friction dampers in diagonal bracing
- Supplemental nonlinear viscous damper configuration:
  - VIII. 20 nonlinear viscous dampers in diagonal bracing

The estimated performance is illustrated in the following figures for each damper arrangement. Figure 14 and 15 show the effects on the structure and on performance of a 68 linear viscous damper configuration I with damper parameters $c_d = 0$, 500, 1000, 1500, 2000 and 3000 ton s/m. Modal damping ratios of the first five modes of vibration are shown as a function of c_d. As Figure 15 shows, the symmetric damper configuration does not control inherent torsion due to structural asymmetries.

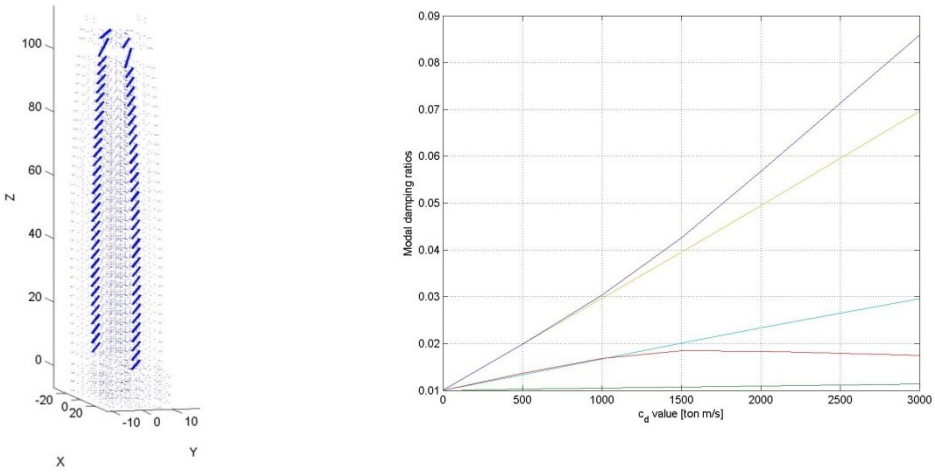

Figure 14 Linear viscous damper arrangement I and modal damping ratios as functions of linear viscous damping constant c_d.

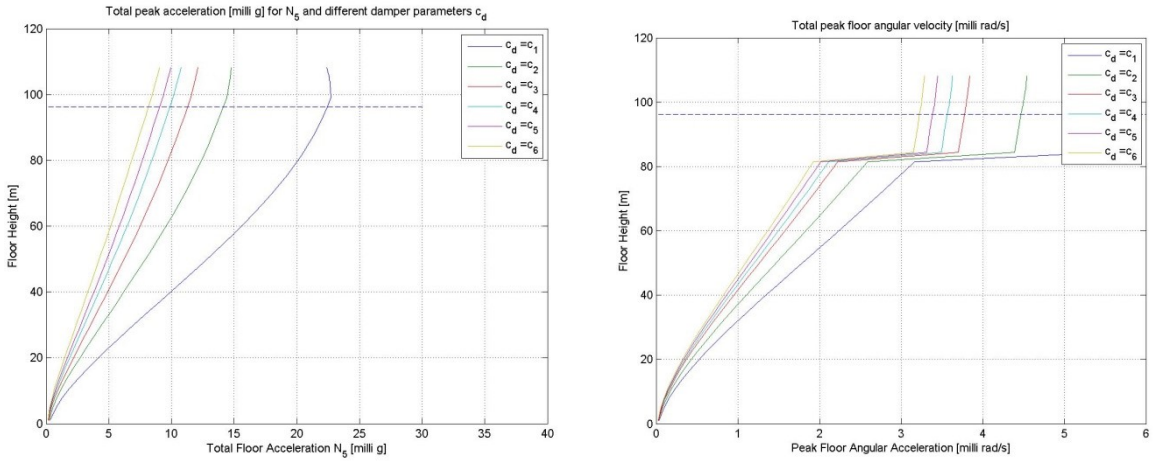

Figure 15 Linear viscous damper arrangement I: estimated PFA and PFV as a function of linear viscous damping constant c_d.

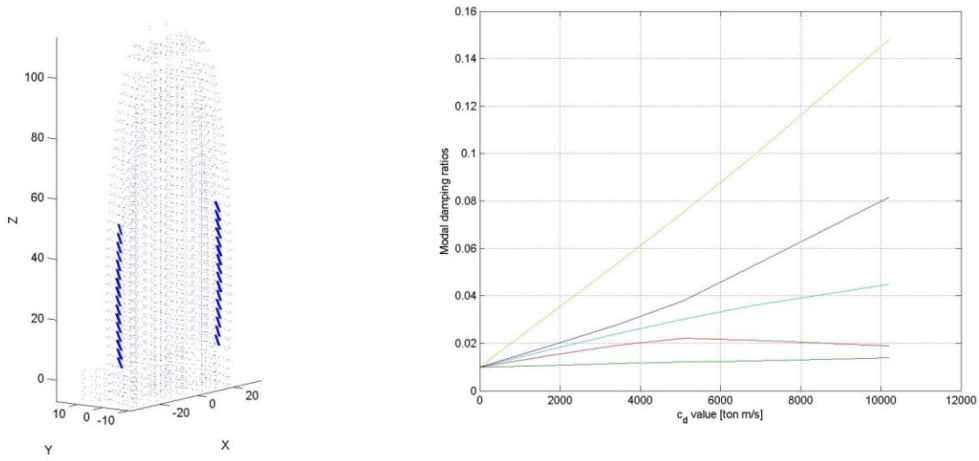

Figure 16 Linear viscous damper arrangement II: modal damping ratios as functions of damping constant c_d.

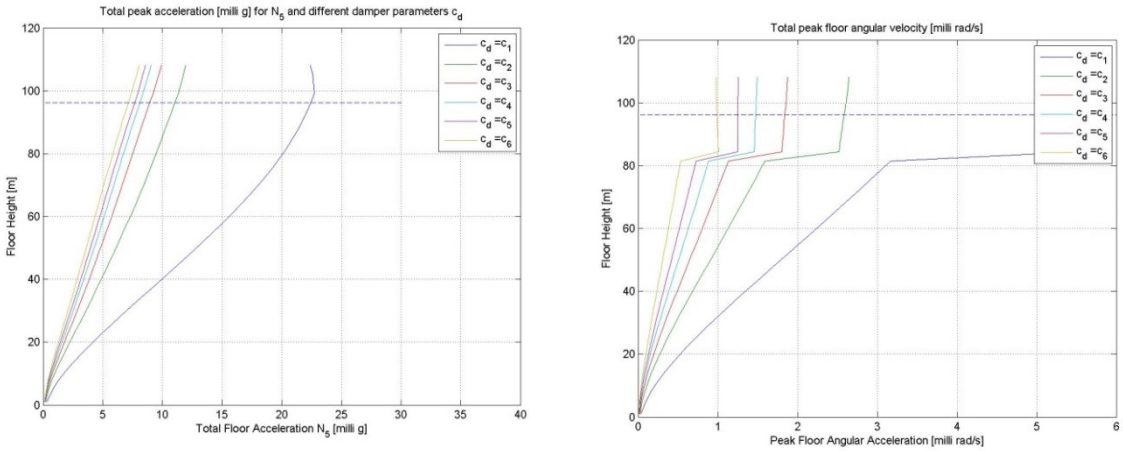

Figure 17 Linear viscous damper arrangement II: modal damping ratios and estimated PFA and PFV as a function of damping constant c_d.

Figures 16 and 17 show configuration II obtained by selection of the 32 location of dampers with larger energy dissipation from arrangement I. Modal damping ratio increments as a function of c_d are shown in Figure 16. Angular velocity performance improves significantly with respect to configuration I (Figure 17). Figure 18 shows estimates of peak forces and peak deformation in 32 viscous dampers in configuration II.

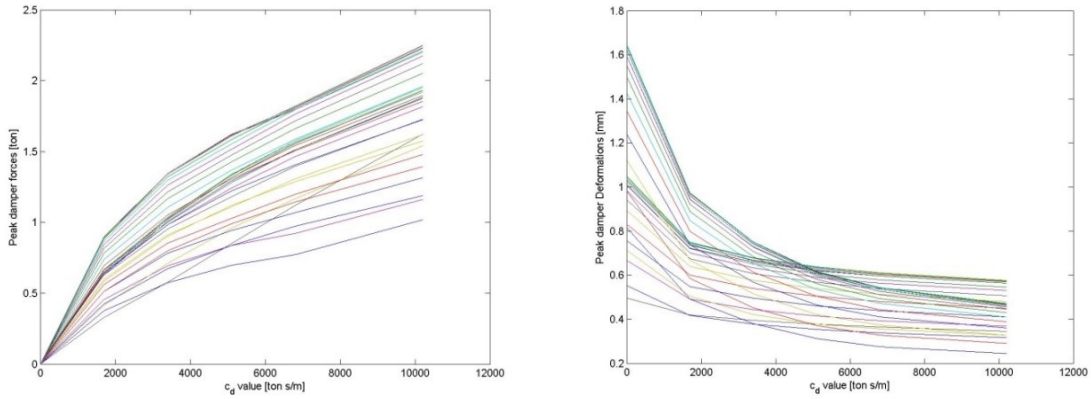

Figure 18. Linear viscous damper arrangement II: modal damping ratios and estimated PFA and PFV as a function of damping constant c_d.

Performance of configuration III is shown in Figures 19 and 20. This configuration was conceived to reduce the number of viscous dampers and analyze the order of magnitude of deformation demands on the diagonal connected every two floors. In this case, $c_d = 0$, 750, 1500, 2250, 3000 and 4500 ton s/m. As in the case of configuration I, this configuration controls peak acceleration but does not control peak floor angular velocity.

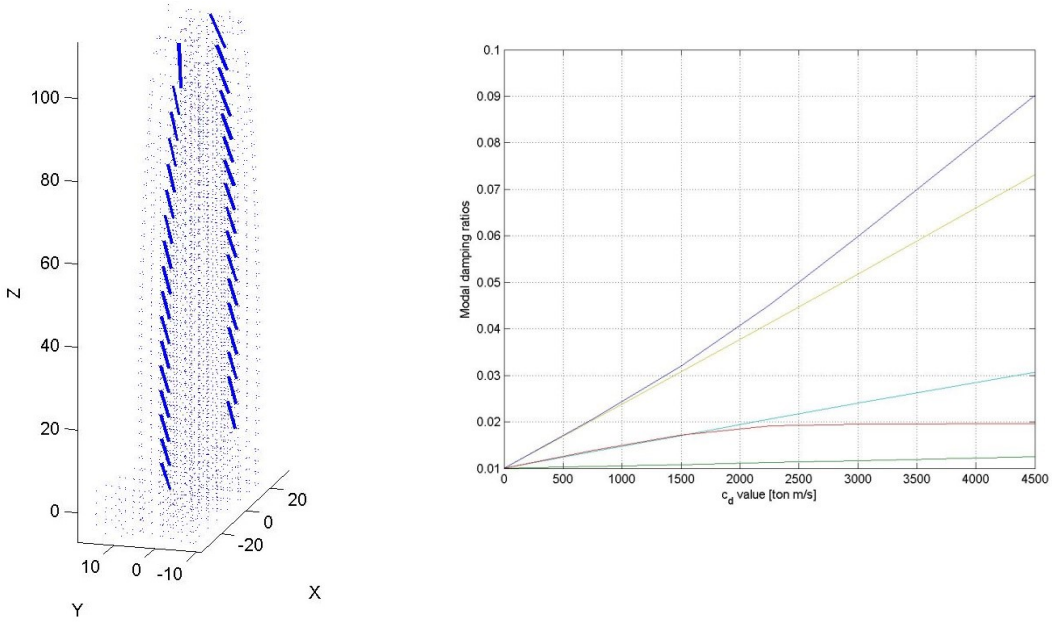

Figure 19 Linear viscous damper arrangement III: modal damping ratios as a function of damping constant c_d for 34 linear viscous dampers.

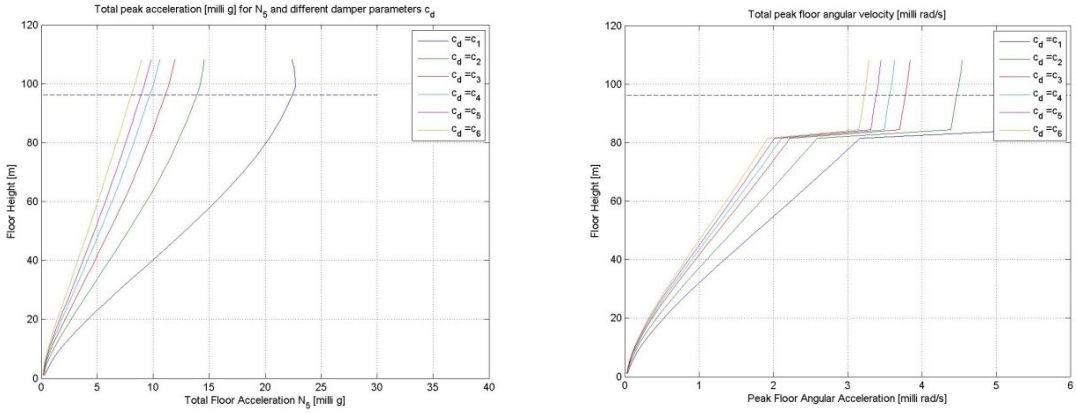

Figure 20 Linear viscous damper arrangement III: estimated PFA and PFV as a function of damping constant c_d.

Selecting the 22 location of dampers with larger energy dissipation from arrangement III, configuration IV was conceived. The performance of this configuration for damper parameters $c_d = 0$, 773, 1545, 2318, 3090 and 4637 ton s/m is shown in Figures 21 and 22. This asymmetric configuration effectively controls floor angular velocities and peak floor accelerations and determines a design with larger damper forces and damper deformations. Figure 23 shows peak deformation and force demand for this configuration in 1-year recurrence win events.

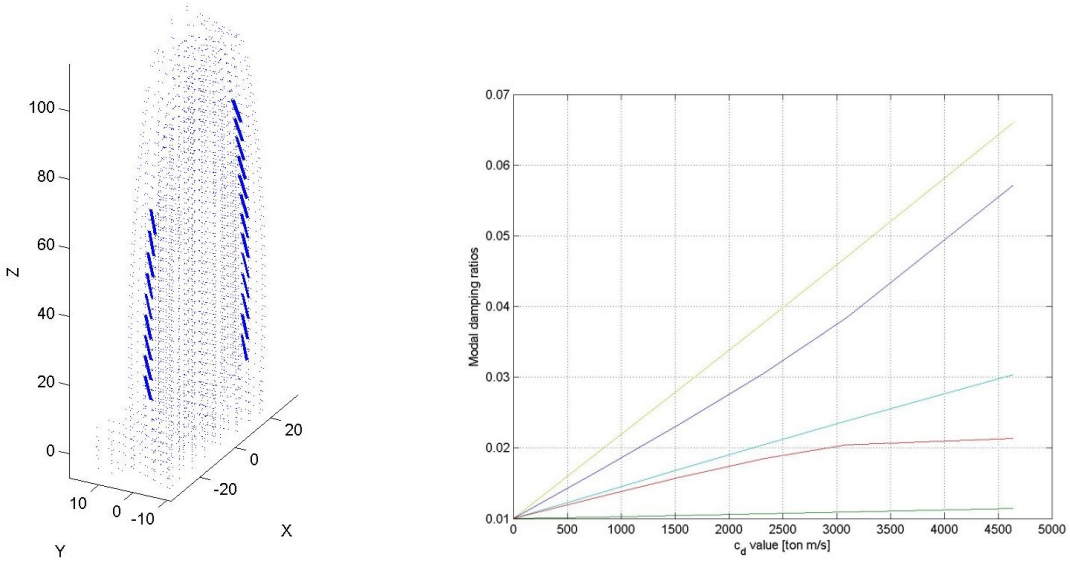

Figure 21 Linear viscous damper arrangement IV: modal damping ratios as functions of damping constant c_d of 22 dampers.

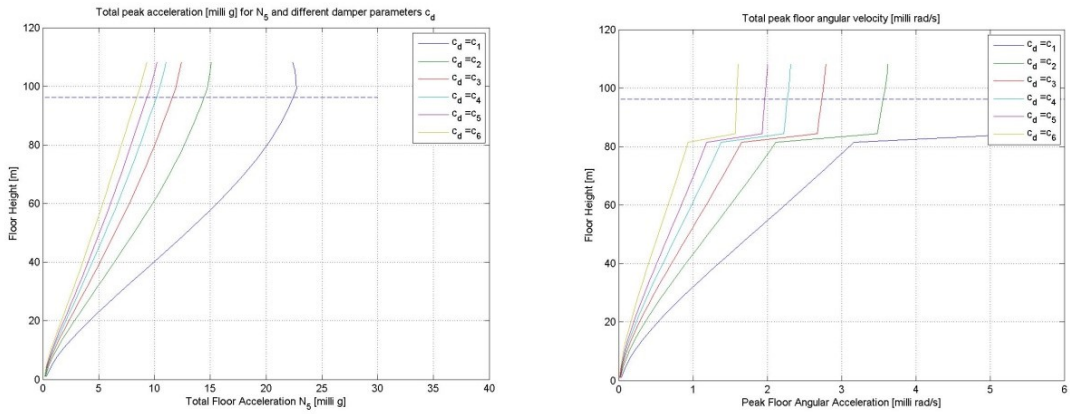

Figure 22 Linear viscous damper arrangement IV: estimated PFA and PFV as a function of damping constant c_d for 22 viscous dampers.

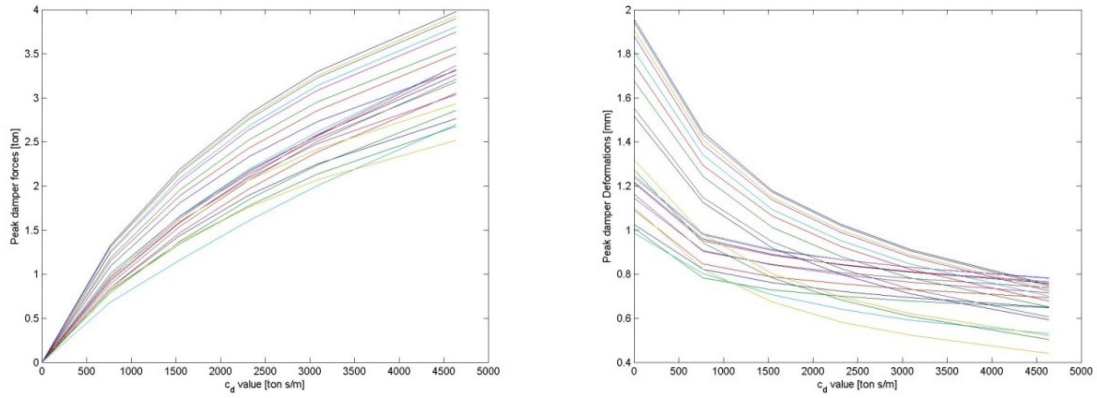

Figure 23 Linear viscous damper arrangement IV: estimated peak forces and deformations as functions of damping constant c_d for 22 viscous dampers.

The performance of configurations V and VI that included additional elastic diagonals did not improve torsional behavior of the building. For brevity these results are not included.

Taking the location of 20 dampers of arrangement III that exhibit larger energy dissipation, configuration VII is conceived using friction dampers, looking for a cost reduction. Friction capacities in the range of 1 to 3 ton (metric tons) with diagonal connectors that deform 0.16 mm for 4 ton axial force. The performance of the building with friction dampers for yield capacities $F_y = 0$, 0.5, 1, 1.5, 2 and 2.5 ton is shown in Figure 24.

Configuration VII with 2 ton capacity friction dampers achieves peak floor accelerations < 10.2 milli g, increasing friction capacity leads to increase in peak total acceleration. This implies that more stringent ISO peak acceleration performance < 7.6 milli g cannot be reached with this configuration of friction dampers. Additional dampers could be added at levels 28-29 to improve dynamic stiffness at weak floor to improve performance.

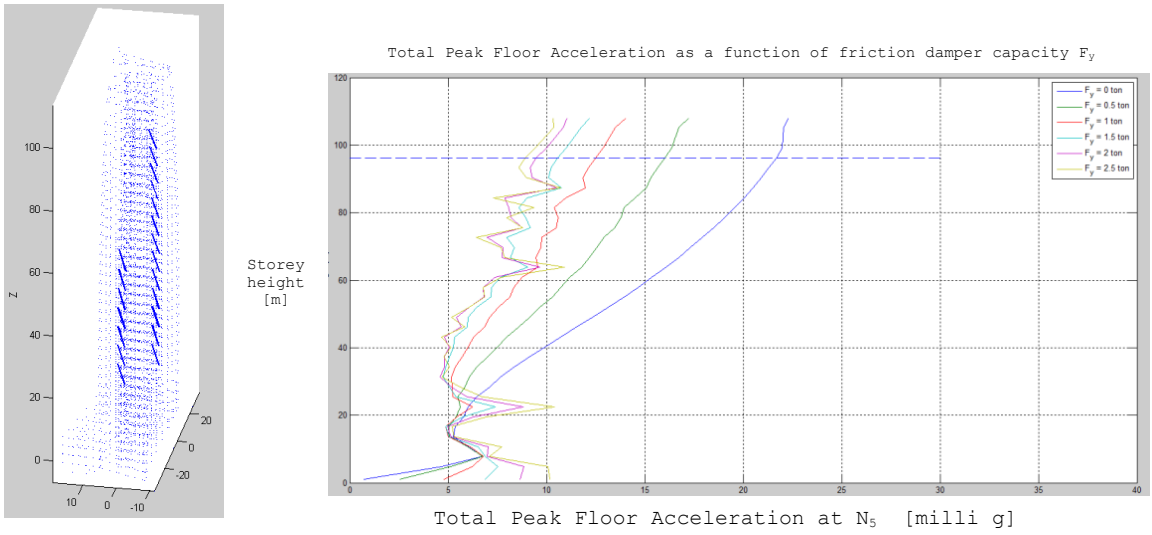

Figure 24 Friction damper arrangement VI: modal damping ratios and estimated PFA and PFV as a function of damping constant c_d.

The last configuration studied was arrangement VII with 20 nonlinear viscous dampers with deformation rate exponent $\alpha = 0.3$. The force in these dampers is modeled as

$$f_d = c_\alpha |\dot{\Delta}|^\alpha \operatorname{sgn}(\dot{\Delta}) \tag{41}$$

where $\dot{\Delta}$ is the deformation rate of the damper.

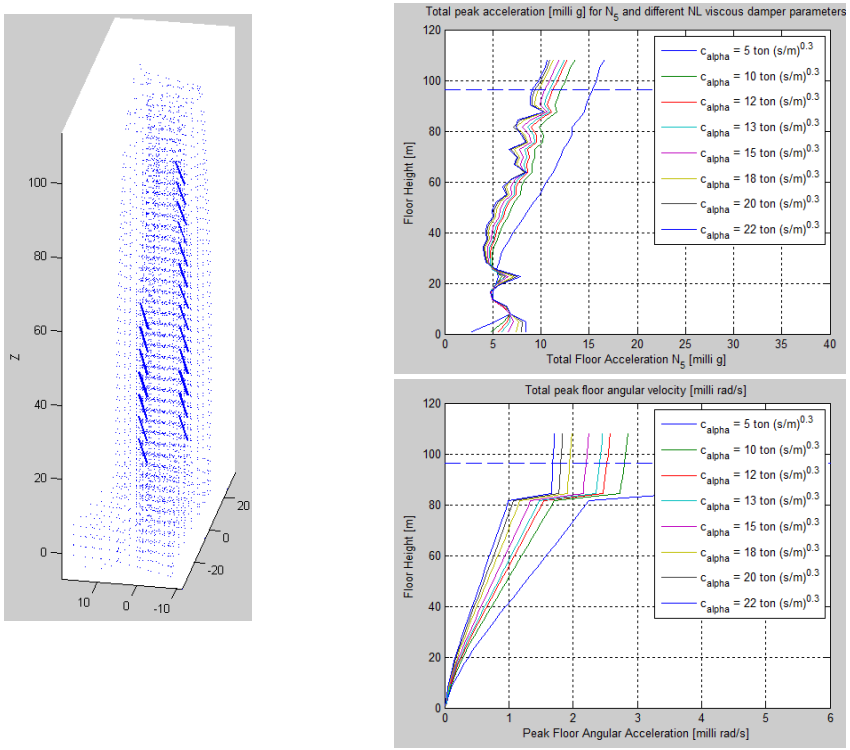

Figure 25 Nonlinear viscous damper arrangement VII: modal damping ratios and estimated PFA and PFV as a function of damping constant c_α.

The performance of the building for different damper constants $c_\alpha = 5$, 10, 12, 13, 15, 18, 20 and 22 ton (s/m)$^{0.3}$ is shown in Figure 25. Values of $c_\alpha > 18$ ton (s/m)$^{0.3}$ would determine relatively high peak forces for extreme wind or earthquake events and this would imply larger y more expensive elastic diagonals. As in previous cases, an additional improvement in angular velocity performance of the higher floors could be obtained with additional dampers at level 28-29.

If Melbourne criterion (10.2 milli g PTFA) is taken as design acceleration performance objective, the friction damper configuration VI provides the most convenient solution because axial loads in elastic diagonals for this case are smaller than those of linear viscous and nonlinear viscous dampers for 1-year recurrence wind events, and significantly smaller than those of linear viscous or nonlinear viscous for extreme wind or earthquake events. This implies minimal cost of structural components that combined with the lower cost of friction dampers of 2.5 ton capacity in relation to viscous dampers with larger capacities.

If ISO more stringent acceleration criterion is selected for the design of supplemental dampers, nonlinear viscous damper arrangement VII would be recommended, because it can provide comparable performance to that achievable with linear viscous dampers but with smaller peak force demand in 1-year recurrence wind events and, more importantly, in extreme wind and earthquake events. The design and cost/performance optimization of the friction or nonlinear viscous damper configuration is a step to be developed in case the structural engineer and the building owner agree on the introduction of energy dissipation devices to improve occupant performance.

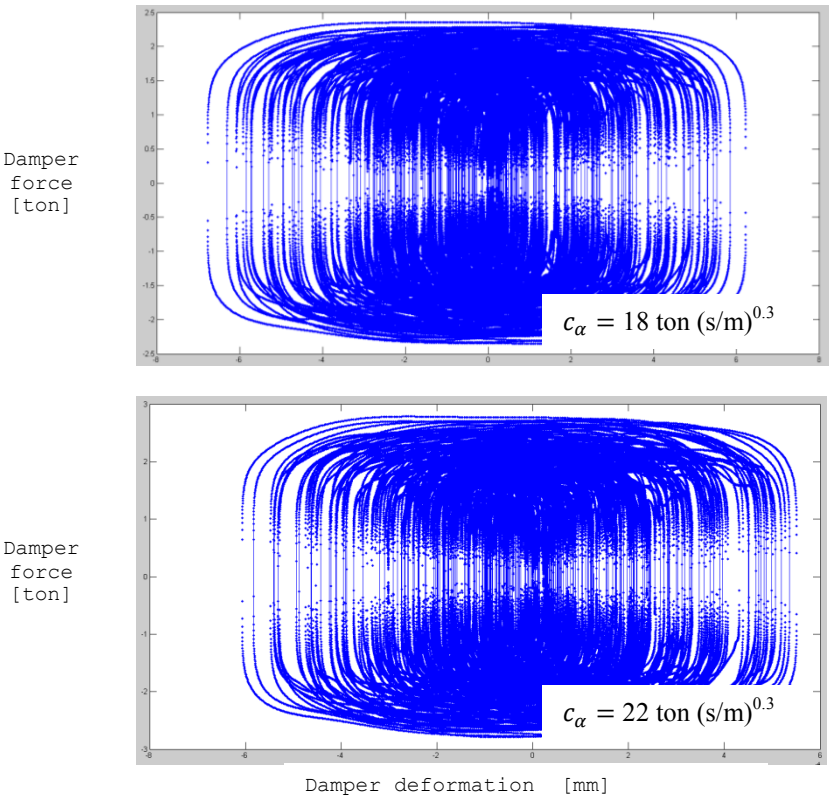

Figure 26 Nonlinear viscous damper arrangement VII: force-deformation hysteresis loops of nonlinear viscous dampers c_α.

8 CONCLUDING REMARKS

Computer fluid dynamics to create a stochastic wind loading model for vibration analysis of a flexible 36-story concrete building has been applied for the preliminary design of supplemental dampers for occupant comfort in one year recurrence wind events. Large-Eddy-Simulation with random turbulence field as inflow boundary condition simulated using Huang's algorithm has been applied for estimating along the wind forces, across the wind forces and torsional moments along the height of the building. The random samples of wind turbulence at the inlet were tested and adjusted by comparing power spectral densities and spatial correlation of the theoretical wind model of the wind defined.

The preliminary design process of viscous and friction dampers using a stochastic wind force model has been reported for a specific building. Performance comparisons were developed by numerical integration of the equations of motion of a reduced-order model with and without dampers subjected to wind force realizations compatible with the wind scenario defined for occupant comfort serviceability level created by LES CFD with random field generation of 3-dimensional turbulence in the inlet of the FE model used to compute wind forces.

Although wind tunnel testing is definitely the most recommendable and most frequently used strategy for extreme load validation in design of tall buildings, computational LES with RFG techniques for performance evaluation in low and high intensity events and supplemental damping design is a valuable strategy in terms of time and cost.

REFERENCES

Codina R., Pressure stability in fractional step finite element methods for incompressible flow, *Journal Computational Physics*, 170 112-140, 2001.

Chorin A., On the convergence of discrete approximation to the Navier-Stokes equations, *Math. Comput*., 23, 1969.

INTI-CIRSOC, *CIRSOC 102 Reglamento Argentino de acción del viento sobre las construcciones*, INTI CIRSOC, Buenos Aires, Argentina, 2005.

ISO 10137, *Bases for design of structures - Serviceability of buildings and walkways against vibrations*.

Kareem A., Dynamic Response of High-Rise Building to Stochastic Wind Loads, *Journal of Wind Engineering and Industrial Aerodynamics*, 41-44, 1101-1112, 1992.

Tamura Y., and Kareem A., editors, *Advanced Structural Wind Engineering*, Springer, Japan, 2013.

Castro G., Paz R. and Storti M., Evaluation of the proper coherence representation in random flow generation based Methods, *Journal of Wind Engineering and Industrial Aerodynamics*, December 2016.

Smirnov, A., Shi, S., Celik, I., Random flow generation technique for large eddy simulations and particle-dynamics modeling, *Journal of Fluids Engineering*, 123, 359-371, 2001.

Kraichnan, R., Diffusion by a random velocity field, *Phys. Fluid*, 11, 43, 1970.

Huang, S.H., Li Q.S. and Wu., J.R., A general inflow turbulence generator for large eddy simulations, *Journal of Wind Engineering and Industrial Aerodynamics*, 98, 600-617, 2010.

Smagorinsky, J, General Circulation Experiments with Primitive Equations, 1963, *Month Weather Review*, 91 (3), 99-164, 1963.